

Towards whole-brain validation of diffusion MRI fiber orientation distributions with x-ray microcomputed tomography

Scott Trinkle, Sean Foxley, Narayanan Kasthuri and Patrick La Rivière

Last edited: May 31, 2018

Note: This document is a loosely-organized collection of everything I have written regarding the validation of HARDI ODFs/FODs with microCT data using structure tensor analysis. Some of it borrows heavily/directly from other papers, most notably Schilling et al. 2018 [1] (validating HARDI with 3D histology) and Alimi et al. 2018 [2] (all of spherical harmonic discussion in section 2.3.2).

1 Introduction

Diffusion MRI (dMRI) is a powerful, non-invasive tool for characterizing three-dimensional (3D) tissue microstructure on a macroscopic scale, and is widely used in both research and clinical settings. New methods of reconstructing 3D fiber orientation distributions (FODs) from dMRI data are rapidly being developed, each based on the assumption that the diffusion contrast from dMRI provides an accurate representation of the underlying anatomical fiber structure. Previous efforts to validate these FODs have relied on ground truth histological data with non-isotropic resolution over small regions of interest (ROI). In this study, we demonstrate a pipeline for the use of natively isotropic, synchrotron-based x-ray microcomputed tomography data to validate FODs over a whole mouse brain.

2 Methods

2.1 MRI

2.1.1 Acquisition

A post-mortem brain was scanned on a Bruker 9.4 T magnet with a 3D diffusion-weighted spin-echo sequence at 150 μm isotropic resolution. Data was acquired at a b-value of 3000 s/mm^2 over 30 uniformly distributed directions.

2.1.2 MRI reconstruction methods

The MRI ODFs were reconstructed from the dMRI data using diffusion tensor imaging (DTI) [3], constrained spherical deconvolution (CSD) [4], Q-ball imaging, constant solid angle (CSA) [5], and the sparse fascicle model (SFM) [6]. All reconstructions were performed using the open-source Dipy Python package [7].

2.2 X-ray

2.2.1 Acquisition

The specimen was then stained with uranyl acetate, osmium tetroxide and lead citrate in preparation for x-ray imaging at the Advanced Photon Source at Argonne National Lab. The x-ray data was acquired using a mosaic stitching method, yielding an image volume over the whole brain with 1.2 μm isotropic resolution.

2.3 Structure Tensor Analysis

Structure tensor analysis was initially developed in a 1987 computer vision paper by Bigun and Granlund [8]. It has since been used for a variety of computer vision and materials science applications, including finding the orientation of textile fibers with synchrotron microCT imaging [9]. It was notably applied to validating diffusion MRI with 2D histology by Budde [10, 11] and others. Schilling [12, 1] and Khan [13] have extended the analysis to 3D for the same purpose.

2.3.1 Derivation

Consider a three-dimensional intensity image, $f(x, y, z)$, with gradient:

$$\nabla f_{\sigma_d} = (f_x, f_y, f_z)^T \quad (1)$$

which is calculated using Gaussian derivative filters:

$$f_x = g_{x,\sigma_d} * f \quad f_y = g_{y,\sigma_d} * f \quad f_z = g_{z,\sigma_d} * f \quad (2)$$

where $*$ denotes the convolution operator and g_{i,σ_d} denotes the spatial derivative in the i -direction of a 3D Gaussian with standard deviation σ_d :

$$g_{i,\sigma_d} = \frac{\partial}{\partial i} \left(\frac{1}{(2\pi\sigma_d^2)^{3/2}} \exp \left\{ -\frac{x^2 + y^2 + z^2}{2\sigma_d^2} \right\} \right), \quad i \in [x, y, z] \quad (3)$$

The image gradient is used to construct a “gradient square tensor” by taking the dyadic product of the gradient vector with itself:

$$\text{GST}_{\sigma_d} = \nabla f_{\sigma_d} \nabla f_{\sigma_d}^T = \begin{pmatrix} f_x^2 & f_x f_y & f_x f_z \\ f_x f_y & f_y^2 & f_y f_z \\ f_x f_z & f_y f_z & f_z^2 \end{pmatrix} \quad (4)$$

Each element of the GST is then averaged over a local neighborhood to create the voxel-wise structure tensor. This averaging is typically performed using a 3D Gaussian filter with standard deviation σ_N :

$$\text{ST}_{\sigma_N}(\nabla f_{\sigma_d}) = g_{\sigma_N} * (\nabla f_{\sigma_d} \nabla f_{\sigma_d}^T) = g_{\sigma_N} * \begin{pmatrix} f_x^2 & f_x f_y & f_x f_z \\ f_x f_y & f_y^2 & f_y f_z \\ f_x f_z & f_y f_z & f_z^2 \end{pmatrix} \quad (5)$$

This results in a 3×3 symmetric, positive semi-definite, rank-two tensor at every voxel. The direction of

minimal intensity variation is given by the eigenvector of this tensor corresponding to the smallest eigenvalue. We make the assumption that this direction also describes the corresponding fiber orientation of that voxel.

The eigenvalues can be used to estimate the certainty in the estimated fiber orientation with a voxel-wise anisotropy measure. Here, we use fractional anisotropy (FA), a metric that is also used in MRI diffusion tensor imaging (DTI):

$$\text{FA} = \sqrt{\frac{1}{2} \frac{(\lambda_1 - \lambda_2)^2 + (\lambda_2 - \lambda_3)^2 + (\lambda_1 - \lambda_3)^2}{\lambda_1^2 + \lambda_2^2 + \lambda_3^2}} \quad (6)$$

where λ_1 , λ_2 and λ_3 are the primary, secondary and tertiary eigenvalues of the structure tensor.

The FA is commonly used to threshold the image f , so voxels with low anisotropy are not included in the orientation distribution.

2.3.2 Construction of X-ray ODF

The structure tensor analysis generates a principal orientation vector at each voxel. Alimi et al. [2] describe how an ODF can be generated over a 3D ROI by binning the vectors from the X-ray data into a spherical histogram expanded on the real spherical harmonics (SH).

The spherical harmonics are defined as

$$Y_l^m(\theta, \phi) = N_l^m P_l^m(\cos\theta) e^{jm\phi}, \quad (7)$$

where N_l^m is a normalization coefficient, P_l^m are the associated Legendre polynomials, and $\theta \in [0, \pi]$ and $\phi \in [0, 2\pi]$ are the polar and azimuth angles, respectively. The SH form an orthonormal basis over $L_2(\mathbb{S}^2)$. Any square integrable function $g(\theta, \phi) \in L_2(\mathbb{S}^2)$ can be expressed as a linear combination of SH:

$$g(\theta, \phi) = \sum_{l=0}^{\infty} \sum_{m=-l}^l c_{lm} Y_l^m(\theta, \phi), \quad (8)$$

with coefficients c_{lm} given by

$$c_{lm} = \int_{\mathbb{S}^2} g(\mathbf{w}) \bar{Y}_l^m(\mathbf{w}) d\mathbf{w}, \quad (9)$$

where the overbar denotes conjugation and

$$\mathbf{w}(\theta, \phi) = [\sin\theta\cos\phi, \sin\theta\sin\phi, \cos\theta]^T. \quad (10)$$

We can model each orientation vector in an X-ray ROI as a Dirac delta function δ on the sphere. That is, in a ROI containing K voxels, our ODF can be written as

$$\text{ODF}(\theta, \phi) = \frac{1}{K} \sum_{k=1}^K \delta(\theta - \theta_k) \delta(\phi - \phi_k). \quad (11)$$

If we substitute this into Eqn 9, then the sifting property of the Dirac delta function can be used, and the

integral reduces to:

$$c_{lm} = \frac{1}{K} \sum_{k=1}^K \bar{Y}_l^m(\theta_k, \phi_k). \quad (12)$$

A SH approximation $\hat{\text{ODF}}(\theta, \phi)$ can then be determined to an arbitrary band-limit L_{max} using Eqn 8.

Spherical harmonics are used extensively in the HARDI literature to represent ODFs [4]. Generally, it is assumed that diffusion is symmetric about the origin, so odd-ordered SH components are assumed to be zero and ignored. Furthermore, since the diffusion-weighted signal and ODF are both real functions, their SH representations exhibit conjugate symmetry:

$$Y_l^m(\theta, \phi)_{real} \equiv \begin{cases} \sqrt{2} \text{Re} [Y_l^{|m|}(\theta, \phi)] & m < 0 \\ Y_l^0(\theta, \phi) & m = 0 \\ \sqrt{2} \text{Im} [Y_l^m(\theta, \phi)] & m > 0 \end{cases} \quad (13)$$

These simplifications hold true for the X-ray ODFs as well. In this work, we use a band-limit of $L_{max} = 20$, for a total number of 231 even-ordered SH coefficients.

2.4 Comparison Metrics

A number of features were calculated from the MRI and X-Ray ODFs. A peak finding algorithm implemented in the Dipy python package [7] was used to identify the orientations of distinct fiber populations. In this algorithm, peaks are defined as points on the ODF that are greater than at least one neighbor and greater than or equal to all neighbors. Peaks are discarded if they are below a threshold percentage of 20% of the maximum peak value and within a minimum separation angle of 20° . These threshold values are commonly seen in the literature [14, 1].

To evaluate agreement in overall shape between ODFs, the angular correlation coefficient (ACC) and Jensen-Shannon divergence (JSD) are implemented. The ACC is analogous to a linear correlation coefficient and can be calculated directly from the SH coefficients of the two ODFs [15]. Given SH coefficients u_{lm} and v_{lm} for two respective ODFs, the ACC is calculated as:

$$\text{ACC} = \frac{\sum_{l=1}^{L_{max}} \sum_{m=-l}^l u_{lm} \bar{v}_{lm}}{\left[\sum_{l'=1}^{L_{max}} \sum_{m'=-l'}^{l'} |u_{l'm'}|^2 \right]^{1/2} \left[\sum_{l'=1}^{L_{max}} \sum_{m'=-l'}^{l'} |\bar{v}_{l'm'}|^2 \right]^{1/2}}. \quad (14)$$

The JSD measures the distance between two probability distributions and has also been widely used in the dMRI literature [16]. The ODFs are projected onto N values equally distributed over a sphere using a Fibonacci sampling algorithm [CITE?]. The JSD is then defined as

$$\text{JSD}(P, Q) = \frac{D_{KL}(P, M) + D_{KL}(Q, M)}{2}, \quad (15)$$

where

$$M_i = \frac{P_i + Q_i}{2}, \quad (16)$$

P_i and Q_i are the magnitudes of the X-ray and MRI ODFs along index $i \in [1, N]$, and D_{KL} is the Kullback-Leibler divergence [CITE?]:

$$D_{KL}(P, Q) = \sum_i P_i \log \left(\frac{P_i}{Q_i} \right). \quad (17)$$

The JSD is bounded between 0 and 1, where lower values indicate greater similarity of distributions.

3 Sensitivity Study

A number of tests were performed to understand the sensitivity of the final X-ray ODFs and identified peaks to the various parameters in the structure tensor analysis pipeline: specifically the choice of the smoothing factors σ_D and σ_N .

3.1 Phantom creation

First, several digital phantoms were created to investigate the effects of different fiber conditions. A sample ROI roughly the size of a single MRI voxel was taken from the X-ray data. K-means segmentation was performed to segment the vasculature and nerve fibers. A sample slice with both vasculature and fiber masks is shown in Figure 1.

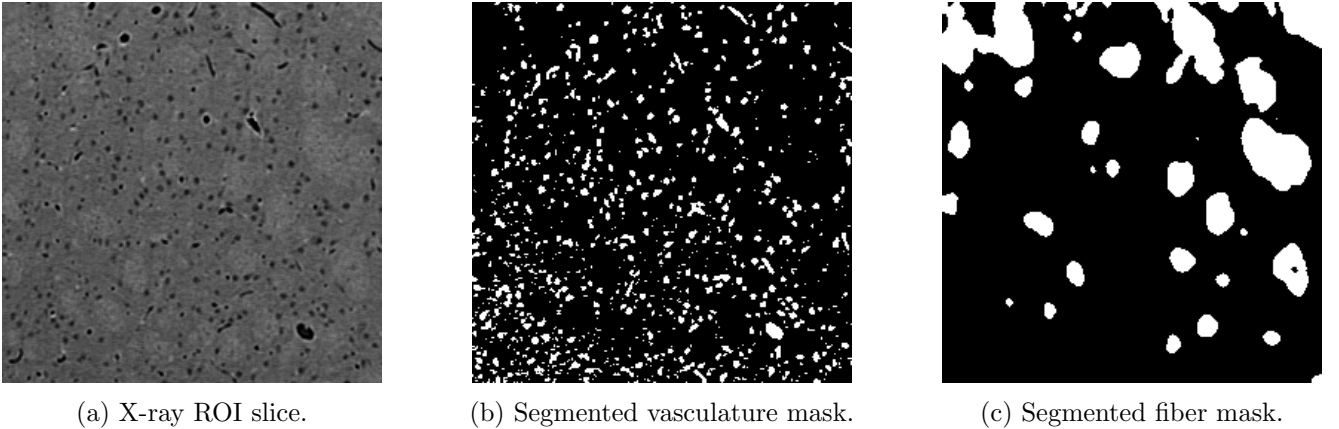


Figure 1: Sample X-ray slice with vasculature and fiber masks.

The simulated $150 \times 150 \times 150 \mu\text{m}^3$ (the size of one MRI voxel) phantoms were then constructed using a random Poisson-distributed background with the same mean as the background in the real data, overlaid with random Poisson distributed values within the raw vasculature mask using the real data vasculature mean, and custom-defined cylindrical nerve fibers, also using random Poisson-distributed values with the same mean as the real data.

Four phantoms were constructed that included nine parallel fibers along the x-axis (left to right in Figure 1a) with radii of 4.8, 9.6, 14.4 and $19.2 \mu\text{m}$, and eight phantoms were constructed that simulated four parallel fibers along the z-axis (in and out of the page in Figure 1a) and four parallel fibers at a specified angle off the

z-axis, from 25° to 85° , every 10° . All fibers in the crossing angle phantoms had a radius of $9.6\text{ }\mu\text{m}$. Sample slices from a 45° crossing fiber phantom and a single fiber population phantom ($r = 9.6\text{ }\mu\text{m}$) are shown in Figure 2.

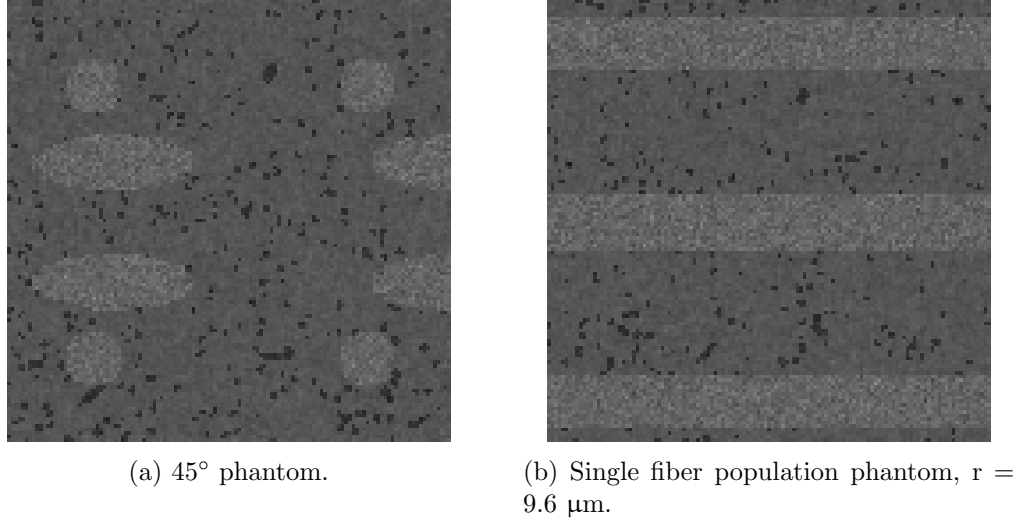


Figure 2: Sample crossing fiber and single fiber population phantoms.

3.2 True phantom ODFs

With the orientations of the phantom fiber populations known exactly, the true ODFs could be calculated and compared with those calculated using structure tensor analysis. For each phantom, the number of voxels in the various fiber population masks was used along with the true orientations of those fiber populations to create a vector of true (θ, ϕ) values. These values were then expanded on SH up to $L_{max} = 20$ as in Equation 12. The true ODFs for the phantoms shown in Figure 2 are shown in Figure 3.

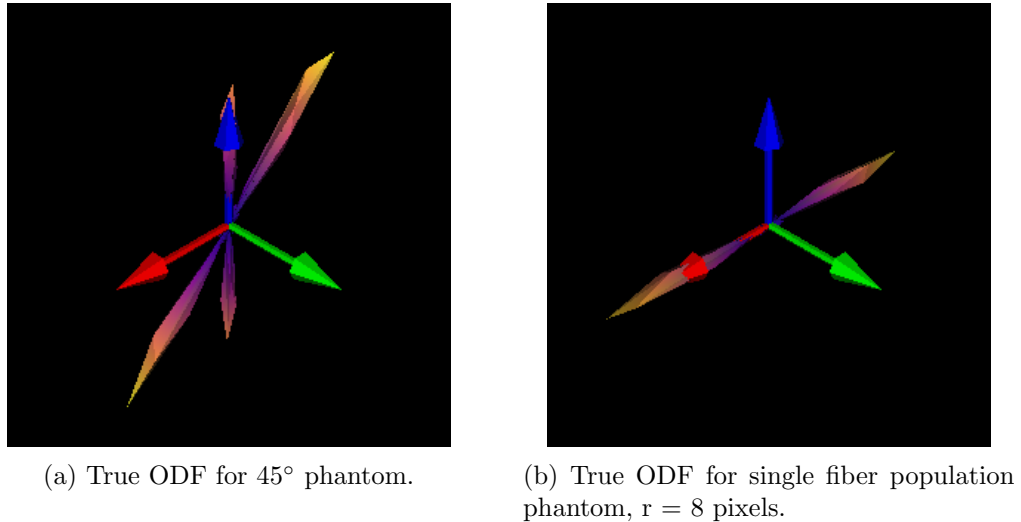


Figure 3: Sample true ODFs for crossing fiber and single fiber population phantoms. SH components were calculated up to $L_{max} = 20$ and represented here on a sphere with $N=1500$ points.

3.3 Comparison with structure tensor ODFs

The ODF was then calculated for each phantom using structure tensor analysis, with values of σ_D from 1–10 μm spaced 0.5 μm apart, and values of σ_N from 2–12 μm spaced 0.5 μm apart, for a total of 399 combinations per phantom.

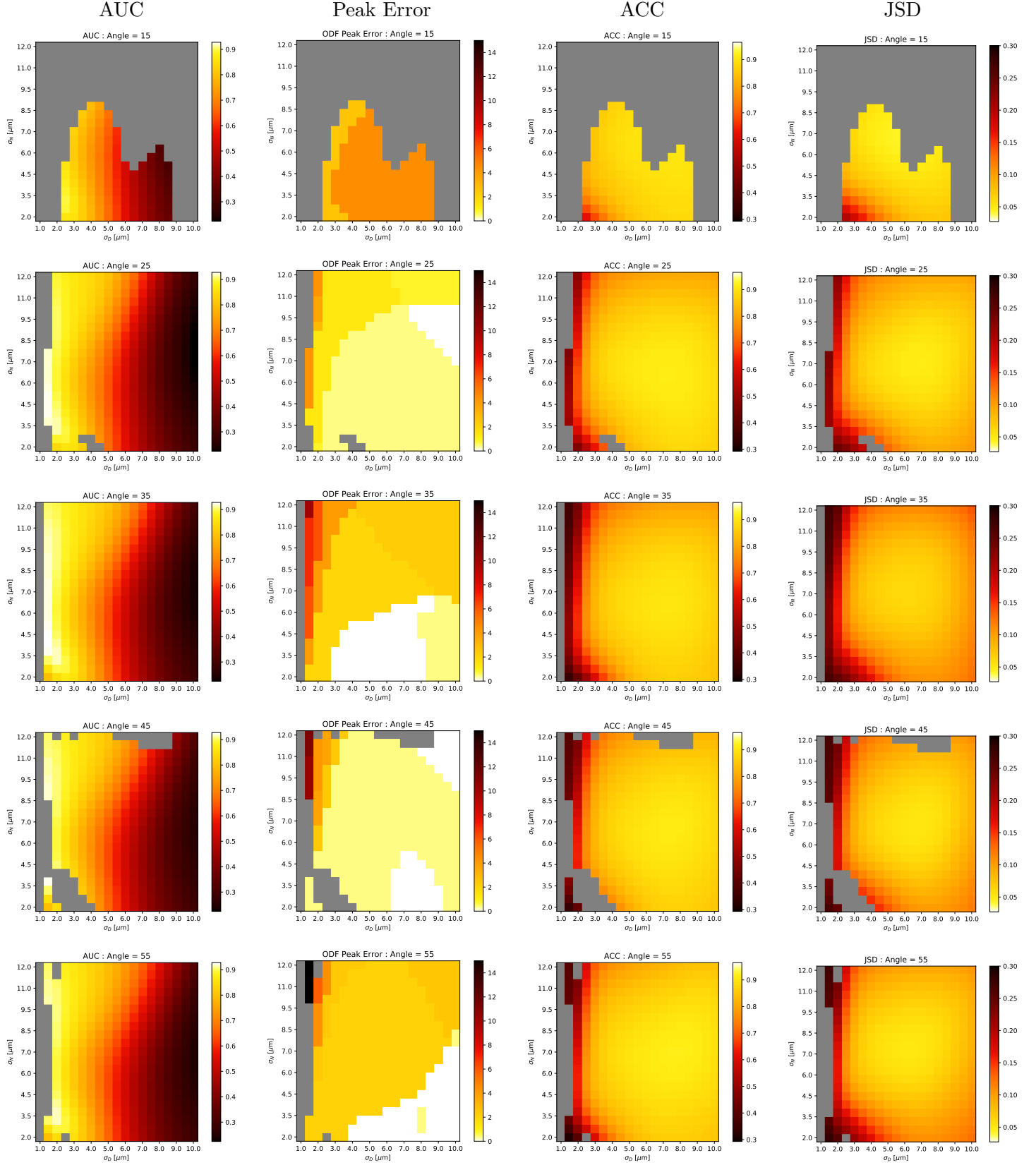
A number of evaluation metrics were calculated for each combination of σ values. The total number of identified peaks was calculated, as well as the angular error between the peak locations calculated from the structure tensor and true ODFs (for the crossing fiber phantoms, the angular error was averaged between the two peaks). The ACC and JSD were used to compare the overall shape of the ODFs. For a good choice of σ values, the voxels within a nerve fiber should have a higher FA value than voxels in the background. To assess this, ROC analysis was performed to evaluate the ability to classify nerve fibers in each phantom by the FA value. The area under the ROC curve (AUC) was then used as an evaluation metric.

Color plots and summary scatter plots of each metric and phantom are shown in Figures 4-5 and 6-7 for crossing fiber and single fiber phantoms, respectively.

For each color plot, σ_D is on the x-axis and σ_N is on the y-axis. Rows from top to bottom indicate either increasing crossing angle or increasing fiber radius. High values are desired for ACC and AUC, while low values are desired for JSD and Peak Error. For ease in visualization, the colormaps for JSD and Peak Error are inverted such that bright/yellow colors indicate good performance across all metrics. Grey pixels indicate combinations of σ_D and σ_N that led to an incorrect identification of the number of peaks in the ODF. The number and location of peaks are key metrics that will eventually be used in comparing X-ray ODFs to MRI ODFs, so these values are excluded.

For the scatter plots, the σ_D , σ_N combination corresponding to the maximum (or minimum, for JSD and Peak Error) metric value are plotted for each metric and each phantom. The color of each point corresponds to either crossing angle or fiber radius, and the shape corresponds to the evaluation metric. Note that some of these metrics do not have a well-defined peak, so the “optimal” choice is somewhat arbitrary.

Figure 4: Parameter evaluation metrics for crossing fiber phantoms. Rows indicate crossing angle between fiber populations. Columns indicate evaluation metrics. Colormaps are inverted for metrics that are desired to be low (JSD and Peak Error)



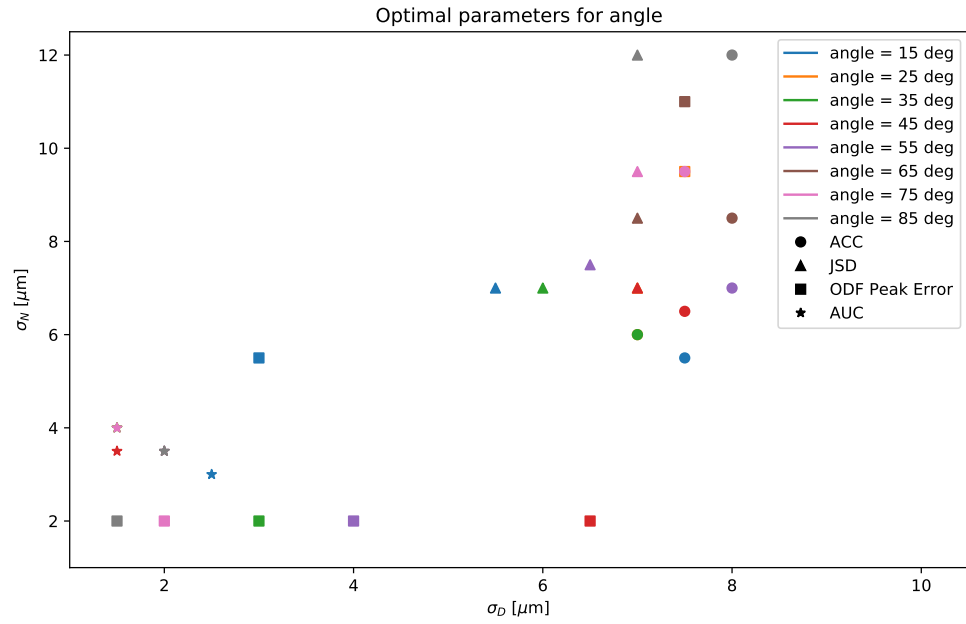
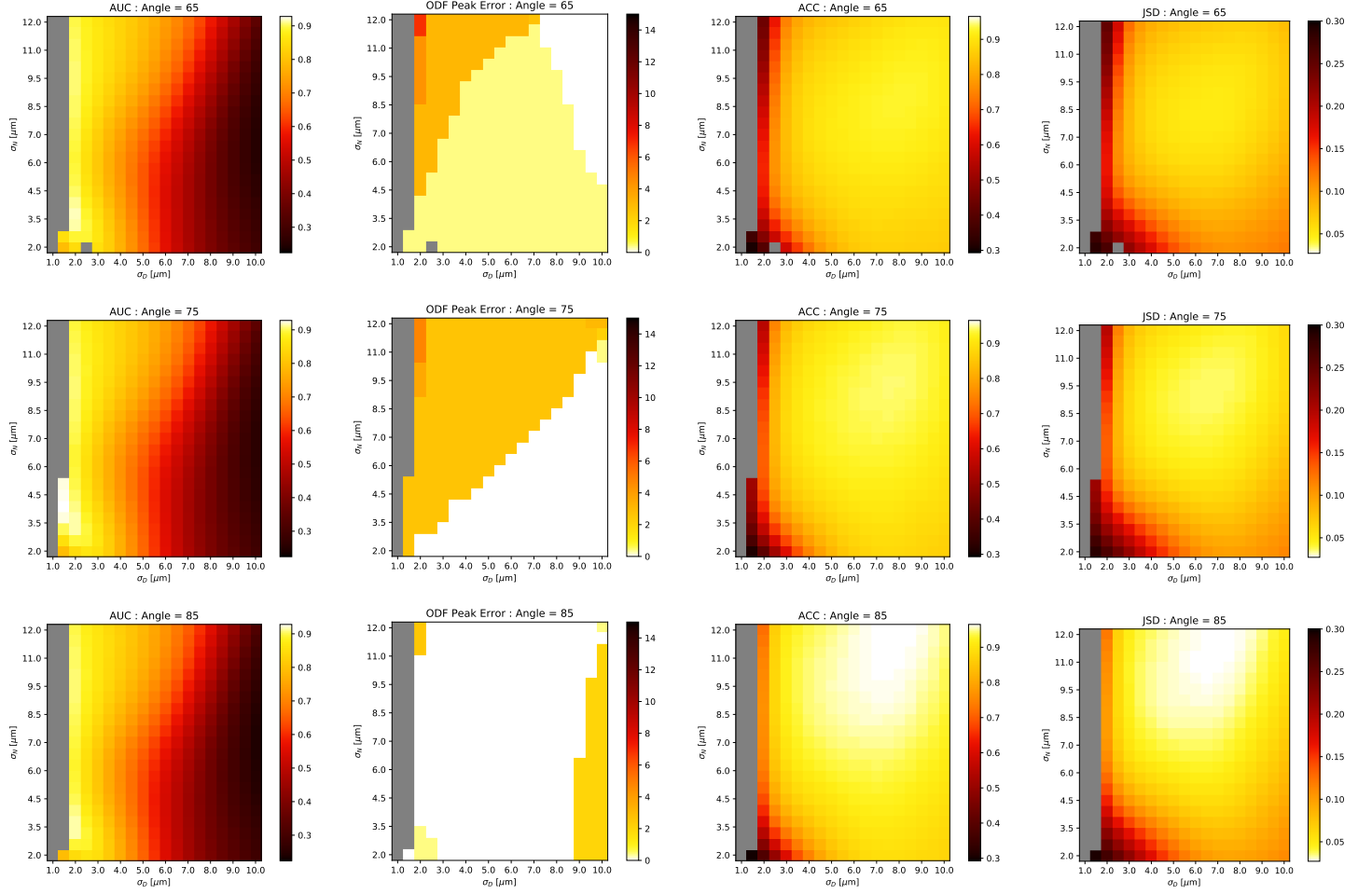
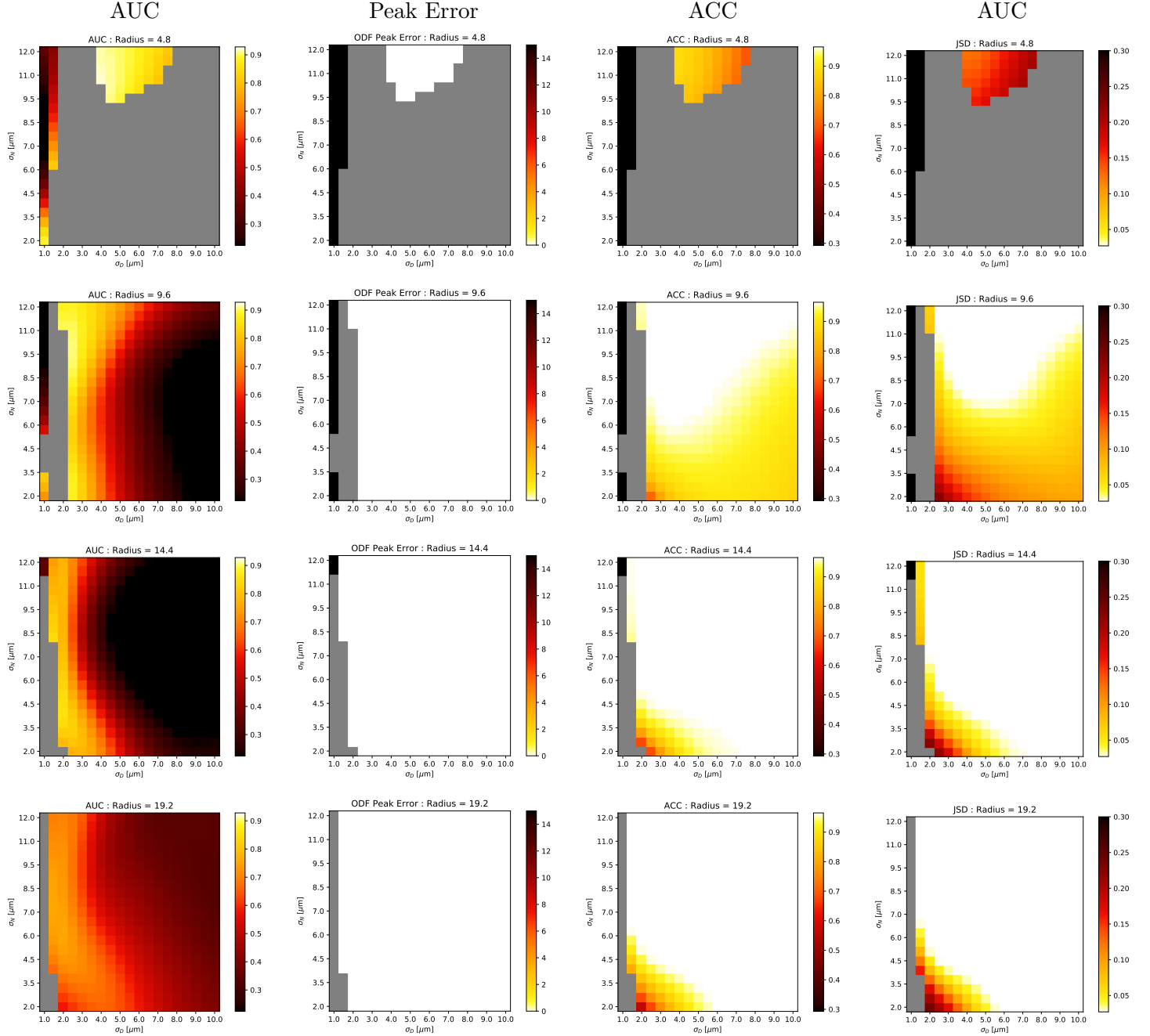


Figure 5: Summary of Figure 4. Each point indicates the σ_D , σ_N pair that maximizes a given metric for a given phantom. Different colors indicate different crossing angles and different shapes indicate different metrics.

Figure 6: Parameter evaluation metrics for single fiber population phantoms. Rows indicate fiber radius. Columns indicate evaluation metrics. Colormaps are inverted for metrics that are desired to be low (JSD and Peak Error)



A few comments about these plots can be made. In general, all metrics are not particularly sensitive to crossing angle or fiber size. The ACC and JSD appear strongly correlated for all phantoms, and also show the most prominent “peak” in the parameter space. This peak is located around $\sigma_D = 7-8 \mu\text{m}$, and around $\sigma_N = 6-9 \mu\text{m}$, with a slight increase in optimal σ_N with higher crossing angles. The ACC and JSD show no trend and extremely low parameter sensitivity for single-fiber phantoms of all sizes.

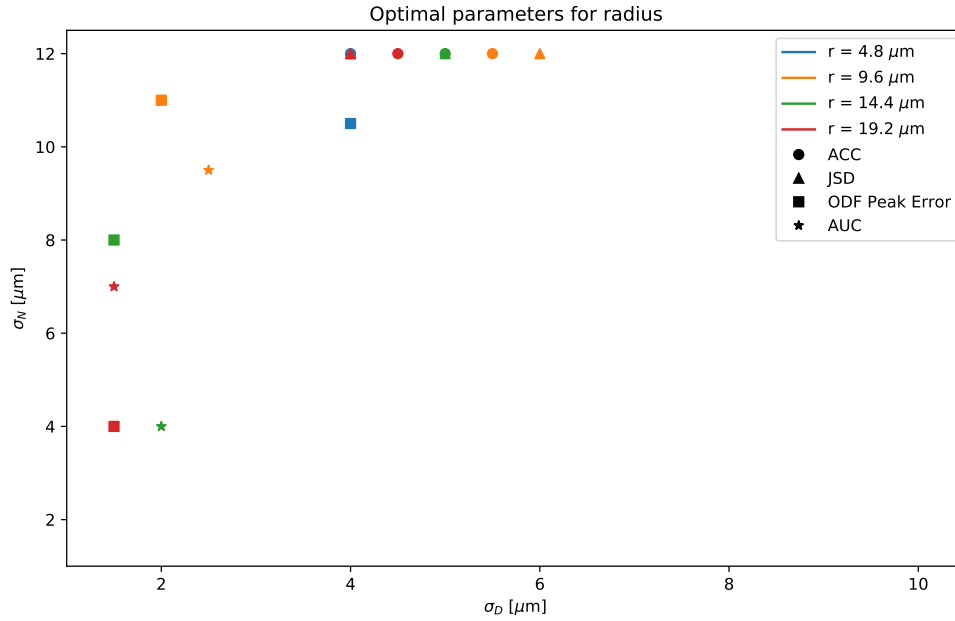


Figure 7: Summary of Figure 6. Each point indicates the σ_D , σ_N pair that maximizes a given metric for a given phantom. Different colors indicate different crossing angles and different shapes indicate different metrics.

The AUC plots show nearly identical trends for all phantoms, but report different optimal parameter selections than the ACC and JSD. There is a less well-defined peak in the AUC plots, and it tends to be located at low σ_D values (1-2 μm) and low σ_N values (3-4 μm). Ultimately, the AUC is based on the FA at each voxel, while the ODFs are constructed from the orientations. For this reason, and since the AUC reports different optimal parameters than the ODF-based metrics, the AUC results can be effectively discarded.

Note that both the JSD and Peak Error metrics depend on the discretization of the sphere. This does not seem to have a large effect on the JSD, as it correlates strongly with the ACC which is independent of spherical sampling. The Peak Error, however, *is* sensitive to the choice of spherical sampling points, which I believe is why the Peak Error plots show discrete regions. These regions do not show any sort of consistent trend across parameter space or crossing angle. Note, however, that for each crossing angle phantom, the Peak Error is generally within 5° for the parameters that maximize the ACC and JSD. Note also that Peak Error does not appear sensitive at all to the fiber radius; it is exactly 0° over nearly all of parameter space for all single fiber population phantoms.

4 Moving forward

With the structure tensor parameters now in place, the following remains to be done:

- Choose FA threshold value
 - Look at the same phantom data to choose the optimal FA threshold value. Voxels with FA below this threshold will be excluded from the ODF.

- Verify HARDI reconstructions
 - I have performed the following reconstructions using the “default values” in the Dipy python package: CSD, Q-ball (CSA), DTI and Sparse Fascicle.
 - Talk with Sean and verify
- **Identify ROI to compare for poster**
 - Will require *some* form of registration.
 - I suggest calculate the linear transform from 5 μm x-ray data to 50 μm structural MRI
 - Apply this data to the 1.2 μm x-ray data
 - Compare ODFs (potentially just qualitatively)

5 Conclusion

This study has demonstrated the feasibility of performing quantitative 3D validation of dMRI FODs with synchrotron x-ray data. This marks the first available ground truth dataset and methodology to allow for whole-brain validation of dMRI FODs with natively isotropic resolution and no sectioning. The application of this analysis to a whole mouse brain will provide a wealth of information regarding the ability of different dMRI algorithms to represent microstructural regions of varying complexity, and will provide the means to perform future large-scale validation studies in dMRI, tractography, and connectomics.

References

- [1] K. G. Schilling, V. Janve, Y. Gao, I. Stepniewska, B. A. Landman, and A. W. Anderson, “Histological validation of diffusion MRI fiber orientation distributions and dispersion,” *NeuroImage*, vol. 165, pp. 200–221, jan 2018.
- [2] A. Alimi, Y. Ussou, J. Pierre-Simon, G. Michalowicz, and R. Deriche, “An Analytical Fiber ODF Reconstruction in 3D Polarized Light Imaging,” in *15th IEEE International Symposium on Biomedical Imaging (ISBI)*, (Washington, D.C.), pp. 1276–1279, 2018.
- [3] P. J. Basser, J. Mattiello, and D. LeBihan, “MR diffusion tensor spectroscopy and imaging,” *Biophysical journal*, vol. 66, pp. 259–67, jan 1994.
- [4] J.-D. Tournier, F. Calamante, D. G. Gadian, and A. Connelly, “Direct estimation of the fiber orientation density function from diffusion-weighted MRI data using spherical deconvolution,” *NeuroImage*, vol. 23, pp. 1176–1185, nov 2004.
- [5] I. Aganj, C. Lenglet, G. Sapiro, E. Yacoub, K. Ugurbil, and N. Harel, “Reconstruction of the orientation distribution function in single- and multiple-shell q-ball imaging within constant solid angle,” *Magnetic Resonance in Medicine*, vol. 64, pp. n/a–n/a, jun 2010.
- [6] A. Rokem, J. D. Yeatman, F. Pestilli, K. N. Kay, A. Mezer, S. van der Walt, and B. A. Wandell, “Evaluating the Accuracy of Diffusion MRI Models in White Matter,” *PLOS ONE*, vol. 10, p. e0123272, apr 2015.

- [7] E. Garyfallidis, M. Brett, B. Amirbekian, A. Rokem, S. van der Walt, M. Descoteaux, and I. Nimmo-Smith, “Dipy, a library for the analysis of diffusion MRI data,” *Frontiers in Neuroinformatics*, vol. 8, p. 8, feb 2014.
- [8] J. Bigun and G. H. Granlund, “Optimal orientation detection of linear symmetry,” pp. 433–438, IEEE, 1987.
- [9] I. Straumit, S. V. Lomov, and M. Wevers, “Quantification of the internal structure and automatic generation of voxel models of textile composites from X-ray computed tomography data,” *Composites Part A: Applied Science and Manufacturing*, vol. 69, pp. 150–158, 2015.
- [10] M. D. Budde and J. A. Frank, “Examining brain microstructure using structure tensor analysis of histological sections,” *NeuroImage*, vol. 63, no. 1, pp. 1–10, 2012.
- [11] M. D. Budde and J. Annese, “Quantification of anisotropy and fiber orientation in human brain histological sections,” *Frontiers in Integrative Neuroscience*, vol. 7, no. February, pp. 1–8, 2013.
- [12] K. Schilling, V. Janve, Y. Gao, I. Stepniewska, B. A. Landman, and A. W. Anderson, “Comparison of 3D orientation distribution functions measured with confocal microscopy and diffusion MRI,” *NeuroImage*, vol. 129, pp. 185–197, 2016.
- [13] A. R. Khan, A. Cornea, L. A. Leigland, S. G. Kohama, S. N. Jespersen, and C. D. Kroenke, “3D structure tensor analysis of light microscopy data for validating diffusion MRI,” *NeuroImage*, vol. 111, pp. 192–203, 2015.
- [14] A. Daducci, E. J. Canales-Rodriguez, M. Descoteaux, E. Garyfallidis, Y. Gur, Y. C. Lin, M. Mani, S. Merlet, M. Paquette, A. Ramirez-Manzanares, M. Reisert, P. R. Rodrigues, F. Sepehrband, E. Caruyer, J. Choupan, R. Deriche, M. Jacob, G. Menegaz, V. Prckovska, M. Rivera, Y. Wiaux, and J. P. Thiran, “Quantitative comparison of reconstruction methods for intra-voxel fiber recovery from diffusion MRI,” *IEEE Transactions on Medical Imaging*, vol. 33, pp. 384–399, feb 2014.
- [15] A. W. Anderson, “Measurement of fiber orientation distributions using high angular resolution diffusion imaging,” *Magnetic Resonance in Medicine*, vol. 54, pp. 1194–1206, nov 2005.
- [16] J. Cohen-Adad, M. Descoteaux, and L. L. Wald, “Quality assessment of high angular resolution diffusion imaging data using bootstrap on Q-ball reconstruction,” *Journal of Magnetic Resonance Imaging*, vol. 33, pp. 1194–1208, may 2011.